Science verification and monitoring layouts for CTAO

DESY Summer Student Programme, 2023

Júlia Laguna Miralles

Universitat Autònoma de Barcelona, Spain

Dr. Victor Barbosa, Dr. Orel Gueta and Dr. Gernot Maier

September 2023

Abstract

The Cherenkov Telescope Array (CTA) is the next-generation instrument in the field of very high energy gamma-ray astronomy. It is set to be composed of two arrays of Imaging Atmospheric Cherenkov Telescopes, located in the northern hemisphere (La Palma, Spain) and the southern hemisphere (Paranal, Chile). They will constitute the CTA Observatory (CTAO). With CTAO still under construction, this project focuses on studying the northern array expected performance at different construction stages (science verification), and the monitoring of different variable sources using sub-arrays (monitoring layouts). To perform the study, we have used the output from Monte Carlo simulations to compute the Instrument Response Functions (IRFs) and sensitivities, using the open-source python package pyirf. We have also simulated observations and extracted light curves using the gammapy package. As a result, a python module has been written to perform the aforementioned study, allowing reproducibility of the workflow. In this report, we will discuss the results for several cases we have examined and provide a link to a public repository containing the code.

Universitat Autònoma de Barcelona
Facultat de Ciències
Departament de Física

Contents

1 Background

The Earth's atmosphere is constantly bombarded by cosmic rays, which consist of high energy particles coming from space. This radiation is produced outside the solar system and mainly consists of charged particles such as electrons, protons and nucleons, and neutral particles such as gamma rays (high-energy photons), neutrinos and anti-neutrinos. When Very High Energy (VHE) cosmic rays enter the Earth's atmosphere, they interact with atmospheric nuclei, creating an avalanche of secondary charged and neutral particles. This avalanche of secondary particles is called an Extensive Air Shower (EAS), with its characteristics depending mainly on the energy, type, and direction of the primary particle (the particle that initiated the shower). If a charged particle goes through the atmosphere, considered a dielectric medium, at a velocity greater than the light phase velocity in the medium, Cherenkov light is generated. In particular, when interacting with the atmosphere, cosmic ray components such as gamma rays and hadrons are known to create secondary particles in their EAS that induce the creation of Cherenkov light through local polarization of the medium around them.

Gamma rays consist of the highest energy expression of light (photons). Due to the presence in space of weak galactic magnetic fields, charged cosmic rays cannot be traced back to their sources. Nonetheless, neutral particles such as gamma rays, as they don't interact with electromagnetic fields, don't experience this phenomena. Hence, gamma ray astronomy is one of the main tools used to study super-energetic cosmic accelerators producing cosmic rays.

Due to the gamma rays EAS interaction with the atmosphere, their study is currently done either through direct detection via space-borne telescopes such as Fermi-LAT [1], or via indirect detection with ground based instruments studying Cherenkov light. Space borne and ground based instruments study complementary energy-ranges, with the latter focusing on the Very High Energy (VHE) regime, above 20 GeV.

Ground based gamma instruments are divided into two categories, particle sampler detectors like HAWC [2], and Imaging Atmospheric Cherenkov Telescopes (IACTs). The latter use a large reflector and a photomultiplier camera to image the Cherenkov light emitted by the charged components of the shower. Examples of these experiments are HESS[3], MAGIC [4] and the upcoming CTAO [5].

1.1 Imaging Atmospheric Cherenkov Telescopes (IACTs)

When a gamma ray (the primary particle) enters the atmosphere, it can induce an electromagnetic EAS of secondary particles started by generating an electron and positron via pair production. Then, bermsstrahlung follows, and an iteration of the two processes is followed until an energy threshold is reached, at which point the EAS dies off. Cherenkov radiation is generated by the charged particles of the EAS as a result of the local polarization of the medium around them. This Cherenkov radiation creates a pool of light that is collected by the IACTs. By reconstructing the shower event, we can gain information of the primary particle, such as its energy and direction [6].

1.2 Cherenkov Telescope Array Observatory (CTAO) - Northern array

The expected improvements of CTAO with respect to previous IACTs experiments are a wider energy range of four orders of magnitude, from 20 GeV to 300 TeV, and an expected improvement in sensitivity of one order of magnitude.

The expected completed configuration of the northern hemisphere array can be seen in figure 1, showcasing two different sizes of telescopes. LST stands for Large-Sized-Telescope, which is set to have 23 meters in diameter and is expected to cover an energy range from 20 GeV to 150 GeV. MST stands for Medium-Sized-Telescope, with 12 meters in diameter and expected to cover an energy range from 150 GeV to beyond 10 TeV. In the present date, only LST01 (figure notation) has already been built.

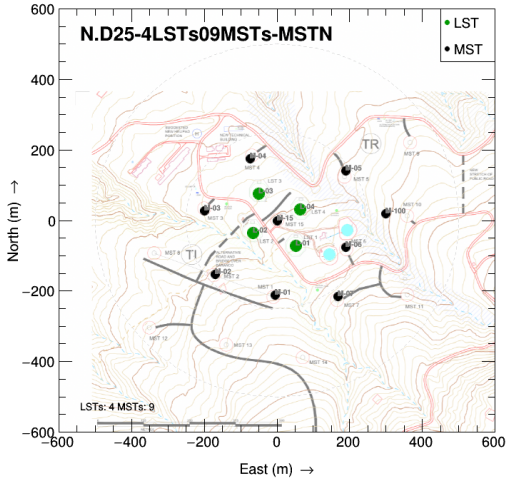

Figure 1: Telescope layout for the northern hemisphere completed array, obtained from [7] (authentication necessary). The layout is known as the D25 or Alpha configuration, consisting of 4 LST and 9 MST, of which only LST01 has already been built. The two additional aquamarine dots stand for the already built MAGIC telescopes.

1.3 Performance criteria

When assessing the performance of the detection of any IACTs, we primarily use what are known as the Instrument Response Functions (IRFs) and the differential sensitivity.

1.3.1 Instrument Response Functions (IRFs)

We will now detail the IRFs used in this project [5].

Background rate

One of the main problems when studying Cherenkov light is that it can be produced as a result of hadronic-induced EAS. Hence, we are at risk of mistakenly attributing a Cherenkov light pool to a gamma ray, when it can have been produced by a hadron

primary particle. The gamma-hadron event recognition, which we use to establish the backgorund rate IRF, is roughly performed in the following way.

When the Cherenkov pool of light reaches the ground, the IACTs inside the pool register the light in their cameras, reconstructing the event and estimating its incoming direction through triangulation of the position and signals recorded by the different telescopes. The shape of these signals in the cameras are elliptical, provided they have been created by a gamma primary particle (unless the shower falls directly above the telescope, in which case we see a circumference). Through image recognition using machine-learning techniques, we can create gamma-hadron selection cuts to discern between gamma and hadron-induced Cherenkov light, as hadronic showers don't produce elliptically-shaped images. This study creates what is known as the signal/background analysis, with which we provide the selection cuts we use in the Background rate IRF. Hence, after presumably identifying the recorded events using the machine-learning derived selection cuts, a measure of high performance in a IACT is when the Background event rate (after selection) is as low as possible.

Effective Area

The effective area or effective collection area can be considered the product of the collection area by the measure of the efficiency of the detector. Hence, it provides information on the amount of gamma rays that hit the atmosphere in the studied area, and how many are we able to reconstruct. In insight, the fact that Cherenkov light creates a big cone of light rends VHE gamma-ray observation feasible from the ground; as despite the low fluxes, detection is possible given the big collection area.

Angular resolution

The angular resolution is the 68% containment radius of the distribution (true-reconstructed) directions. Thus, we seek angular resolution values as small as possible.

Energy resolution

The energy resolution $\Delta E/E$ is obtained with the difference between the reconstructed and true energy, all divided by the true energy of the gamma-ray events recorded by CTAO. $\Delta E/E$ is the half-width of the interval around 0 which contains 68% of the distribution. Therefore, a smaller energy resolution value for different energies indicates a higher instrument performance when reconstructing events.

1.3.2 Differential sensitivity

The flux is the amount of radiant energy received by unit of time and area. With it, the differential sensitivity is the minimum flux required by our instrument to obtain a 5-standard deviation detection of a point like source, calculated in non-overlapping logarithmic energy bins (five bins per decade). In our case, we will also require at least ten detected γ rays per energy bin, and a signal/background ratio of at least 1/20. Overall, by its definition we observe that a higher instrument performance requires low sensitivity

values. Additionally, we must take into account that as the background cuts depend on the duration of the observation, the sensitivity will also depend on this parameter.

1.4 Gamma-ray data treatment

To compare data from different telescopes and sites, VHE gamma-ray astronomers have developed open-source data-analysis tools and standardised data formats. These data formats contain lists of detected photons with their estimated physical observables (energy, direction, ...) and a characterisation of the response of the system. In figure 2 we can see a schematization of the different data levels, which have the following main characteristics:

- Data Level 0 (DL0): Raw data that contains the signal sampled from the photomultipliers of the camera when a trigger event happens (pixel-wise information).
- Data Level 1 (DL1): Calibrated data that contains the pixelated image of the Cherenkov light of the shower (camera-wise information).
- Data Level 2 (DL2): Parametrization of the image with few geometrical quantities in order to determine the observables of the original shower, including its probability of being a gamma-ray shower.
- Data Level 3 (DL3): The detected events are gathered in a list of gamma ray candidates, together with the IRFs.
- Data Level 4 (DL4): This information can be used to perform a statistical analysis obtaining the so-called science products (e.g differential sensitivity plots, light curves...).

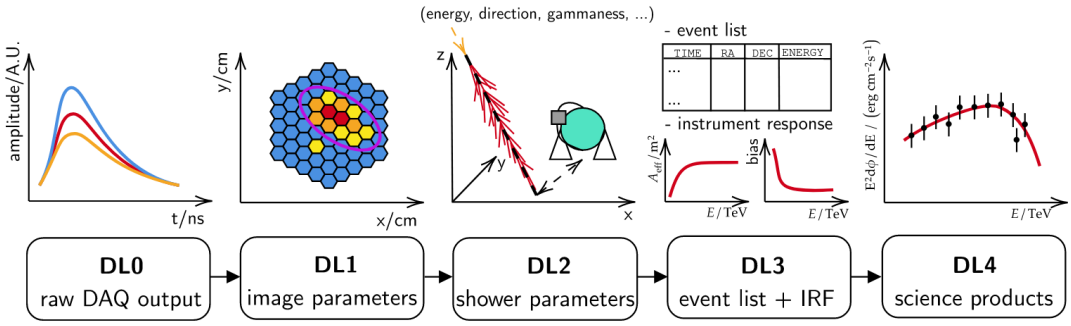

Figure 2: Schematisation of the progressive data reduction and data levels of an IACT, figure obtained from [8].

The information stored in the data levels 3 and 4 is considered high-level data, meaning that it is independent of the detection technique, calibration and analysis methods. For this project, we will go from data level 2 to 3 and 4.

2 Goals

This project has been divided into two main goals, both with a focus on studying the expected performance of the CTAO northern array in La Palma, Spain.

- Science verification of the construction phase: Our aim is to create a pipeline to asses the expected performance at each construction phase. We are looking to answer questions such as which science can be performed during different construction phases, and determining how the construction order can influence early results.
- Assess the performance of monitoring layouts for variable sources: Our aim is to create a pipeline to find the best sub-array of telescopes (monitoring array) to monitor a certain variable source, while also seeking to limit the loss in performance for the telescope array that is left to conduct regular observations (the complementary array). Hence, when we perform the monitoring layout study, we take the Alpha configuration and divide it into the monitoring and complementary array, assessing their separate performances. An example of a possible separation is shown in figure 3.

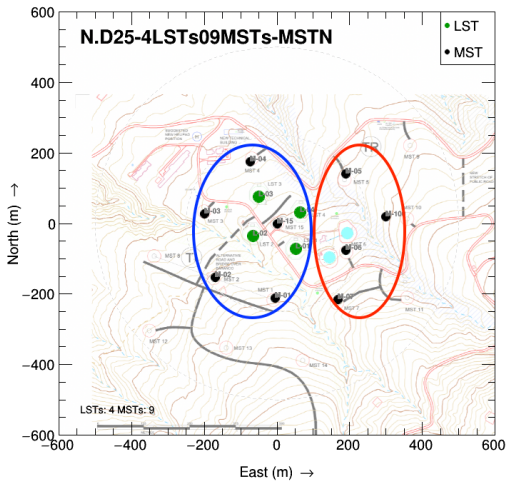

Figure 3: Possible complementary-monitoring array set up. The red ellipse limits the telescopes of the monitoring array, and in blue we have the left-over configuration, which we name complementary array.

3 Methodology

3.1 Monte Carlo simulations

IACTs, as already described in section 1.1, use the atmosphere as the gamma ray detector mechanism, so that the instruments detect the Cherenkov radiation instead of the gamma rays themselves. Given that the CTAO has not yet been built, we don't have observational data with which to perform our studies. Hence, we use Monte Carlo simulations with

two clear differentiated sections. The first sections creates an EAS simulation using the CORSIKA generator, and the second section simulates the telescope detection response, using the sim telarray simulation package. The details for the two packages are provided in [9].
Both simulation sections results have been obtained from model [10], for the different sub-arrays of the CTAO northern hemisphere. The results have provided data level 2 information with which to start our study.

3.2 Science verification

To compare the performance of the array at different construction phases, we have implemented a pipeline that takes the Monte Carlo simulation results for the sub-arrays we want to test, and obtains as a result different metrics that allow us to compare performances.

3.2.1 Array comparison for general observations

To go from the second to the third data level, we have used the pyirf package [11] to obtain the IRFs [12] and differential sensitivity, with the code devised for this project being stored in the following github repository: Summer Project. Pointing out the main characteristics, we have used on-source data with zenith angle of 20 degrees, observation times of 30 min, 5 hours and 50 hours, with the wobble parameter for all cases set to 0 degrees (the gamma-ray source is considered to be in the center of the field of view).

Additionally, as a criterion to select the sub-array with the considered best performance in sensitivity, we have used the Performance Per Unit Time (PPUT) introduced in [13]

$$PPUT = \Big(\prod_{i=1}^{N} \frac{F_{sens,ref}(i)}{F_{sens}(i)} \Big)^{1/N} \tag{1}$$

where $F_{sens,ref}(i)$ and $F_{sens}(i)$ are the reference and achieved differential sensitivity of a point-like source (located in the centre of the field of view) in the ith energy bin, and N is the number of energy bins. By definition, higher PPUT values correspond to better sensitivities in the considered energy range.

In our case, we will consider the Alpha configuration, shown in figure 1, as the reference sensitivity. Hence, the Alpha configuration will have a PPUT value of 1, while all others sub-arrays will have PPUT values between 0 and 1, with higher values indicating better performance.

The final selection criteria for the science verification study has been, according to the concepts described in the previous sections, the following:

- Highest PPUT value with respect to the Alpha configuration (differential sensitivity).
- Low angular and energy resolution values (IRFs).
- High effective area (IRFs).

3.3 Monitoring layouts

For the monitoring layouts section, the devised pipeline follows a different structure. Our aim in this section is to find the best sub-array to monitor a specific variable source. We use the term 'specific' to highlight that the resulting best monitoring layout will depend on the source and flare we are trying to detect. As already commented, we seek to control the trade off between looking for a high-monitoring array performance, and a minimum impact on the complementary array performance that is left to conduct regular observations.

To study the complementary array performance, we will follow a similar procedure to the one used in the Science Verification section. From the Monte Carlo simulations results, we will compute the IRFs and differential sensitivities for the complementary arrays we want to test. Then, we will assess their loss of performance using as the metric the PPUT values described in section 3.2.1.

To study the monitoring array performance, one could think that we could use the same method of comparison and compute their PPUT for the differential sensitivity. Nonetheless, we cannot use this approach here, as we are not aiming to establish the expected performance of this sub-array for a general point-like source (which is the one used to obtain the sensitivity), but for a specific variable source (like a particular AGN or binary). For this reason, we have used the gammapy [14] package to devise the following approach.

First, we have simulated the spectra of the variable source we wanted to study. Then, we have computed the IRFs of the monitoring arrays to test, using the same code devised for the Science Verification study. With these two data sets, we have simulated the expected detection that we would obtain for this variable source and each monitoring array, and we have extracted the light curves. Finally, we have fit the expected detection data points to recover the original source, and with their results, we have devised a metric to compare performances.

Before detailing each step, we must comment that from now on, the full code devised for this project can also be found in the github repository Summer Project, having used the open-source Python package gammapy to go from the third to the fourth data level. Here we will only comment on the main details used to obtain the results shown in this report.

3.3.1 Variable source spectra simulation

We will detail the characteristics used for the Mrk 421, but the code is written so that the parameters can be easily changed to study a different source.

For assessing the monitoring layouts performance, we have simulated the variable source of Mrk 421, an AGN (Active Galactic Nuclei) blazar. To do so, we have used both a spectral and temporal model which we have later joined to obtain the full spectra, without having defined a space model nor a sky map, being a one dimensional simulation. For the parameters of the source, we have used the indicative values shown in table 1. The differential flux $\frac{dN}{dE}$, with N the number of particles and E the energy, depends on the area and time, and is typically fit with a power law. For this case we have assumed it followed

the next expression:

$$\frac{dN}{dE} = \phi_0 \Big(\frac{E}{E_{ref}} \Big)^{-a} \tag{2}$$

Where ϕ_0 accounts for the amplitude normalization, E stands for energy, E_{ref} is the reference energy used to normalize, and a, for our case, will be what is known as the spectral index. What these values mean and their relationships are detailed in [15] in equation 3. As a remark, the flux usually decreases so fast during flares, that it is plotted multiplied by E^2 to better visualize the event characteristics.

Regarding the decay time parameter used in the gammapy temporal model, it indicates that by that value, the flux intensity will have decreased to around 37% of its initial value.

The true energy ranges that have been used are from $10^{-2.5}$ to 10^2 TeV with 40 bins in

Model	Parameter	Value	Frozen
Spectral	Spectral index	2.2	False
	Amplitude	$2 \cdot 10^{-10}$ cm^{-2}s^{-1}TeV^{-1}	False
	Reference energy	1 TeV	True
Temporal	Decay time	6 hours	False
	Reference time (t_{ref})	2020-03-01 (date)	True

Table 1: Parameters used to simulate the spectra and flare of Mrk 421, obtained from TevCat [16]. The parameters that are not frozen indicate that they will be the ones whose values will be searched for during the fitting process.

between, and from 10^{-2} to 10^1 TeV with 10 bins for the reconstructed energy axis. These values have been chosen to cover the full range reached by both the MSTs and LSTs, and the reconstructed axis covers a narrower range than the true axis, as we expect to not be able to detect all edge energies with our telescopes, due to their technical limitations. The source has been simulated as if being located at the center of the camera, with all events happening within the stated true energy axis.

3.3.2 Expected detection and light curve extraction

Once we have the simulated spectra of the variable source, we have computed the IRFs of the monitoring arrays we want to test with the procedure described in section 3.2.1, with the results shown here being for observation times of 5 hours. Then, taking into account both the simulated spectra and the IRFs for the monitoring arrays, we have simulated the expected detection we would attain with the monitoring arrays. The observation parameters used to simulate the expected detection for the results shown in this report are recorded in table 2.

From the simulated detected data, we have also extracted the light curves for the energy bins between 0.01 TeV, 0.3 TeV, 0.6 TeV, 1.0 TeV and 10 TeV. They have been chosen so that we can observe the whole range of energies covered by both the MSTs and LSTs.

Observation parameters	Values
Number of observations	10
Start times between each observation	$t_{ref} + [1, 2, 3, 5, 8, 10, 20, 22, 23, 24]\cdot$ hours
Exposure time for each observation	$[55, 25, 26, 40, 40, 50, 40, 52, 43, 47]\cdot$ minutes

Table 2: Parameters used to simulate the observation. The gap in the times between the sixth and seventh observation account for the day light period. These values have been set taking into account that we will be working with IRFs obtained setting observation times of 5 hours for all tested arrays.

3.3.3 Fitting

Finally, we have taken the expected detection data points, and fitted them to regain the original source spectra. The characteristics of the fit employed can be consulted in the github code, which on a first approach, I would suggest using for all variable sources to test, as it is the approach indicated by gammapy to yield better results [17].

To be able to compare the performance between different monitoring layouts, we have compared their negative $\log \mathcal{L}$, with $\mathcal{L}$ being the likelihood. We have deemed that the monitoring array with the best performance is that which presents the lowest -$\log \mathcal{L}$ value.

3.3.4 Mathematical comment

With this procedure, we are fitting the same model to different data sets, comparing non-nested configurations. Hence, before continuing we must clarify that we cannot properly use the $\log \mathcal{L}$ ratio test as a method for comparison, as this method is used for comparing the goodness of fit with the same data set being fit with different models, not the same model fitting different data sets. Hence, we have used the - $\log \mathcal{L}$ only as our qualitative method for comparison, assessing how well a configuration reproduces the same variable source, but with the clear distinction in mind that we cannot treat the differences in -$\log \mathcal{L}$ as a test statistic, nor compute the p-value and extract significances for our results.

Additionally, another point worth mentioning is that gammapy uses random seeds to initialize the simulations. Hence, each time we run a simulation for the same variable source, monitoring and complementary array, we attain slightly different results. Nonetheless, we have studied the differences between gammapy simulation runs for our situation, and they are significantly smaller than the differences between different monitoring arrays. As a result, we have deemed it not necessary to run the simulation multiple times for each case, as the differences do not signify.

3.3.5 Overall comparison

The goal for the monitoring layouts section is to assess which sub-array configurations (monitoring array) will be better to observe certain variable sources, seeking a trade-off between high monitoring array performance and minimum impact on the complementary array performance (the sub-array configuration that is left to conduct regular observations). Hence, we assess the performance of the complementary array with the PPUT value, and the performance of the monitoring array for the tested variable source with the

-log $\mathcal{L}$ value. To control the trade-off, we are seeking complementary-monitoring arrays pairs that achieve a high PPUT value and a small -log $\mathcal{L}$ value at the same time.

4 Results

From now on, when we express our results in ratio terms, we will be using as reference the values obtained for the Alpha configuration.

4.1 Construction phase study

We will now detail some of the obtained results when comparing different telescope configurations from [7] (authentication necessary).

4.1.1 Two LSTs layouts

In this section we will compare the performances for three differently placed layouts with 2 LSTs each one. In figure 4 we showcase their differential sensitivity, differential sensitivity ratio and energy resolution, alongside the results obtained for the Alpha configuration.

The differential sensitivity is plotted multiplied by E_{reco}^2 (for the reasons stated in section 3.3.1) against E_{reco} in the x-axis, where E_{reco} stands for reconstructed energy. It can be read in the following way: for the given reconstructed energy on the x-axis, we see the E_{reco}^2 times the flux sensitivity value, required in our instrument, to be able to detect the event with the particulars described in section 1.3.2. The y-axis is plotted in $erg \cdot cm^{-2} s^{-1}$ units, but to provide a more intuitive measure, the values in terms of the Crab Nebula flux measured by MAGIC are also drawn in gray lines, so that the reader can easily observe the comparison. The results (indicative values) for the PPUT values for each configuration are shown in the bottom right corner of the plot.

In addition, figure 5 shows the angular resolution, background rate and effective area in terms of the reconstructed energy, also showcasing their ratios plots with respect to the Alpha configuration.

When studying the obtained results, we can see that all 2-LSTs layouts attain similar behaviours, with all of them presenting acceptable and similar IRFs results. SV01c obtains a slightly higher PPUT value, and similar IRFs results compared to the other layouts. Hence, we could consider the SV01c configuration to have the best performance, although the results between all configurations are remarkably similar.

On this matter, we have seen that when comparing these set-ups, the performance doesn't vary much regardless of the two LSTs layout we are able to use at each moment. Nonetheless, in figure 6 we see that this is not the case when comparing different 2 MSTs layouts. In the figure, we show the differential sensitivities for four different 2 MSTs plausible within the Alpha configuration. We hypothesize that their remarkable difference in PPUT values relies in the fact that the distances between MSTs amongst the different layouts vary significantly. As a result, and also checking with the IRFs (can be obtained with the provided code but are not shown here for space reasons), we can conclude that SV04d clearly attains worse performance results. This result can be understood when looking at

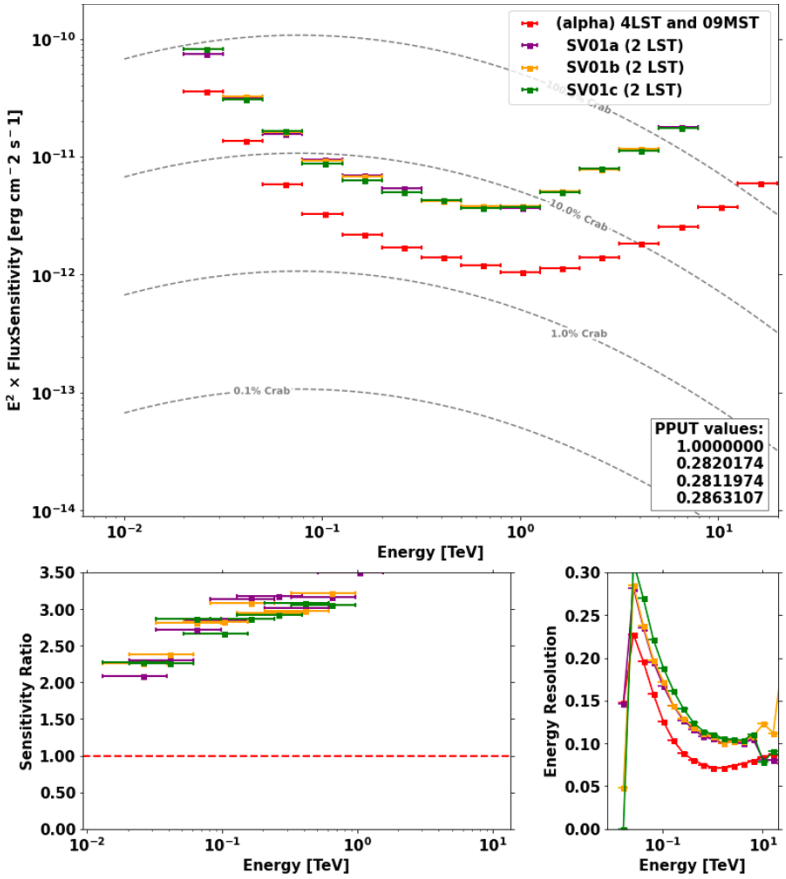

Figure 4: Differential sensitivity per reconstructed energy to the square, plotted against reconstructed energy, differential sensitivity ratio with respect to the Alpha configuration and energy resolution against reconstructed energy. All plots show the results for the Alpha configuration and the three different 2 LSTs layouts, with an observation time of 5 hours.

its geographical disposition, found in [7] (authentication necessary), as its two MSTs are significantly apart.

4.1.2 Performance evolution between 2, 3 and 4 LSTs layouts

In figure 7 we can observe the differential sensitivity, differential sensitivity ratio and the energy resolution for the 2 LSTs layout deemed in the previous section to attain the best performance (SV01c), a nested 3 LSTs layout and a 4 LSTs layout, also showing the results for the Alpha configuration. The results for the IRFs of background rate, angular resolution and effective area are shown in figure 8.

With these plots we clearly observe how does the performance improve when adding more LSTs, simulating the construction phase evolution.

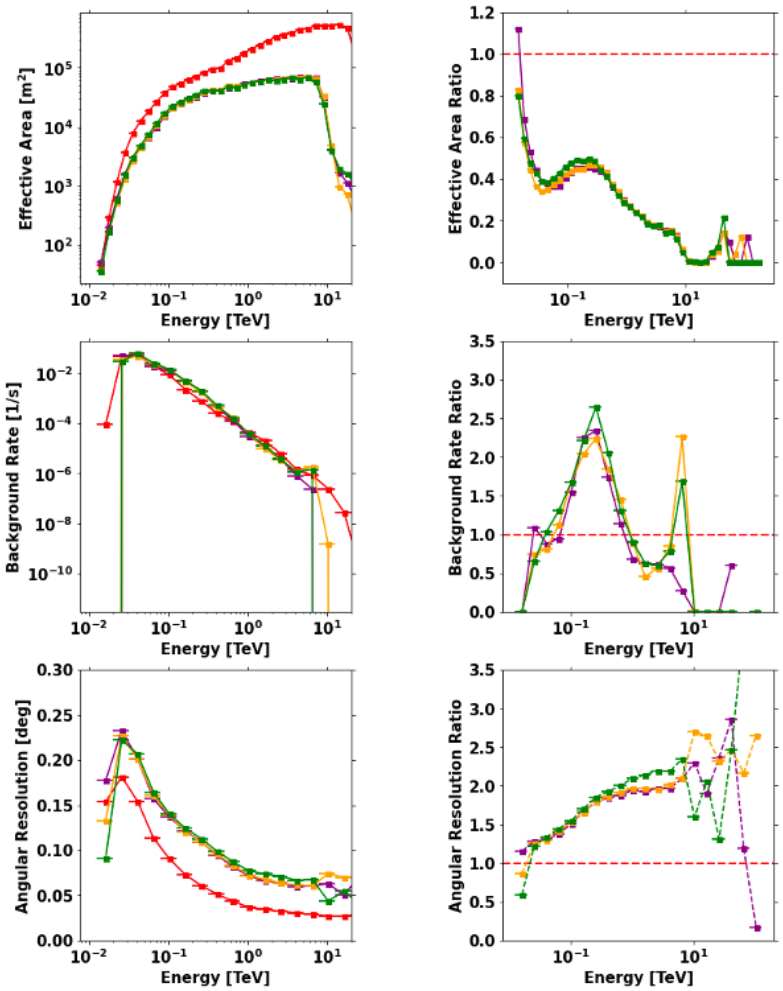

Figure 5: Effective area, background rate and angular resolution plotted agains reconstucted energy, alongside their ratios with respect to the Alpha configuration. All plots show the results for the Alpha configuration and the three different 2 LSTs layouts (with the same legend as in figure 4), with an observation time of 5 hours.

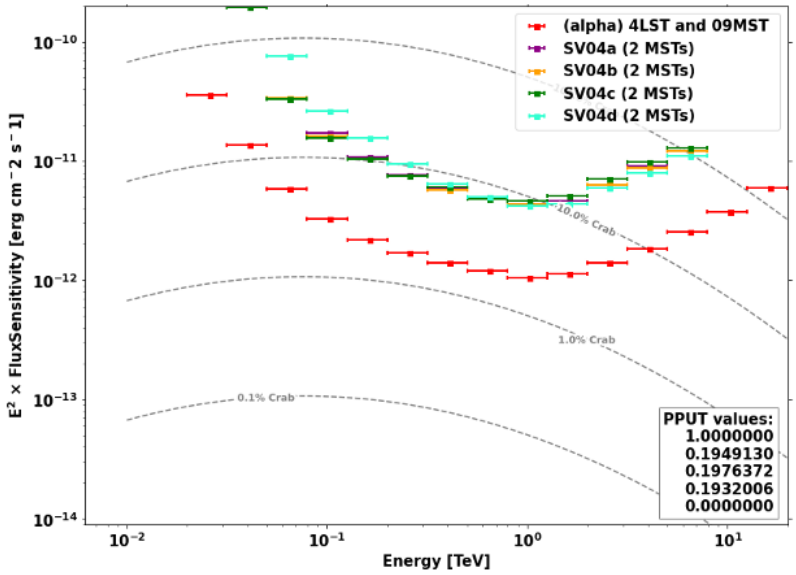

Figure 6: Differential sensitivity per reconstructed energy to the square, plotted against reconstructed energy, for the Alpha configuration and the three different 4 MSTs layouts, with an observation time of 5 hours.

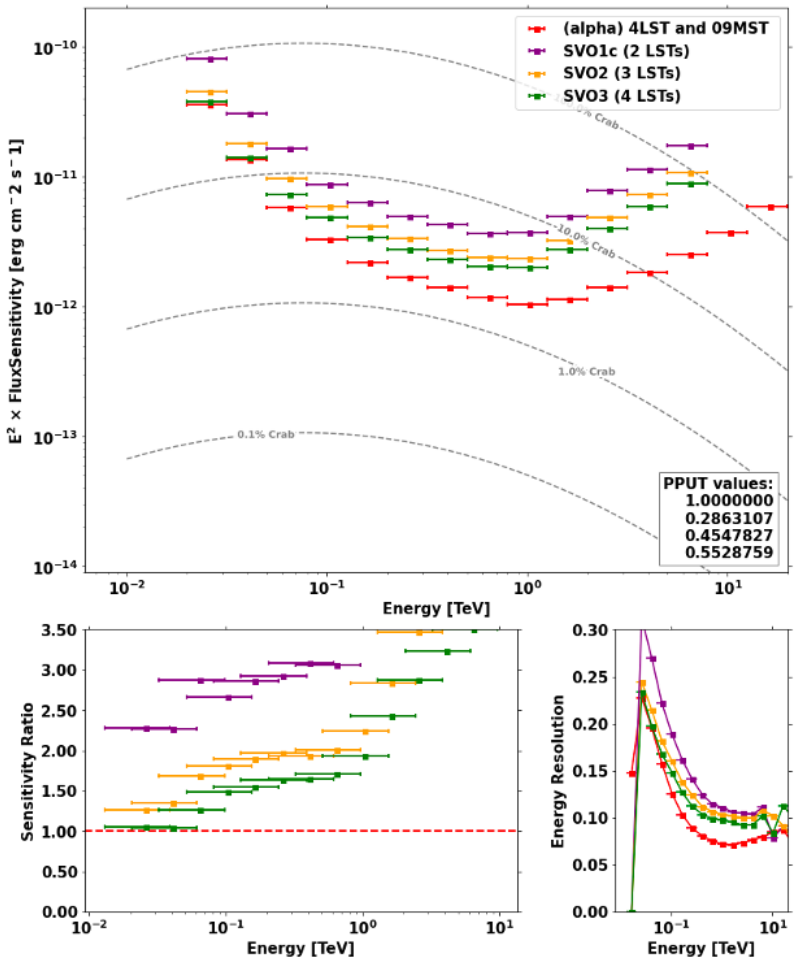

Figure 7: Differential sensitivity per reconstructed energy to the square, plotted against reconstructed energy, differential sensitivity ratio with respect to the Alpha configuration and energy resolution against reconstructed energy. All plots show the results for the Alpha configuration and the best performance 2 LSTs layout, and subsequent 3 and 4 LSTs each layouts, with an observation time of 5 hours.

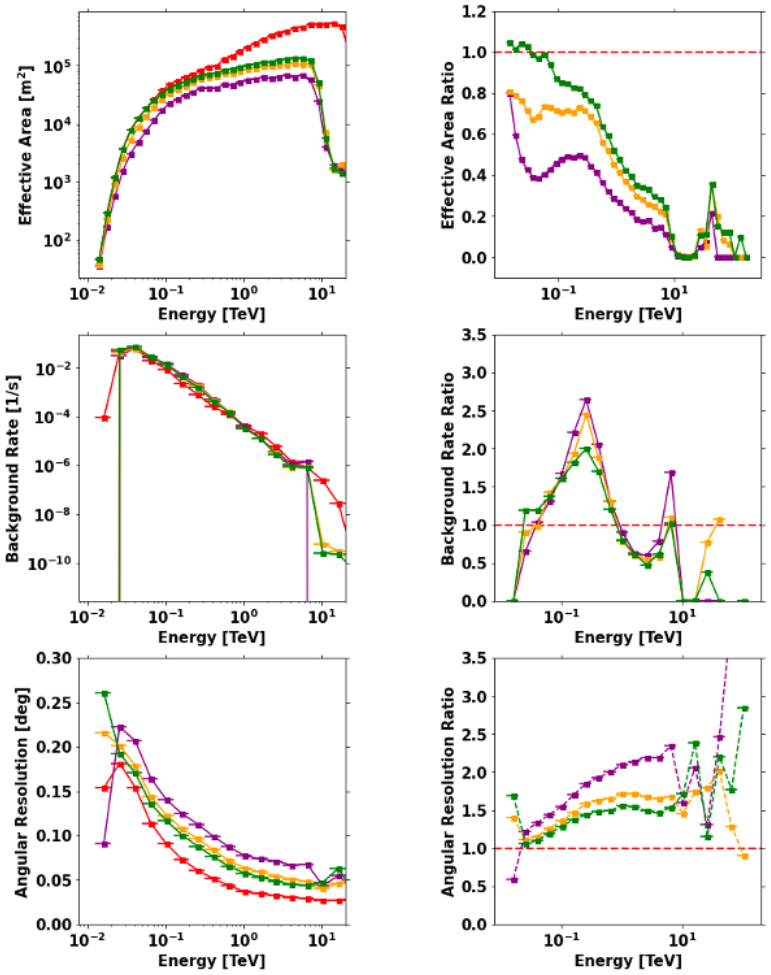

Figure 8: Effective area, background rate and angular resolution plotted against reconstucted energy, alongside their ratios with respect to the Alpha configurations. All plots show the results for the Alpha configuration and the best performance 2 LSTs layout, and subsequent 3 and 4 LSTs each layouts, (with the same legend as in figure 7), with an observation time of 5 hours.

4.2 Monitoring layout for a Mrk 421 flare with a 6 hours time decay

To perform the study for this blazar we have tested 13 different sets of monitoring-complementary arrays. Their types and number of tested sets are recorded in table 3. We have not tested as many different configurations with a lot of MSTs as with fewer MSTs, as it is unlikely that we will have availability to perform monitoring with more than 3 MSTs, because of the loss in performance in the complementary array. We also see

MSTs for monitoring	Tested configurations	Color in figure 10
2	4	Blue
3	3	Orange
4	3	Green
5	1	Red
6	2	Purple

Table 3: Type and number of different monitoring layouts tested for Mrk 421, together with the color in which they are plotted in section 4.2.2.

that we are only testing monitoring layouts with MST, and none with LSTs. This is done because energy ranges and FOVs (Field Of Views) differ between MSTs and LSTs, so we focused our efforts with working using MSTs for the monitoring array. We will now only present the full case study for the four different 2 MSTs monitoring layouts, and we will show the final comparison with all sets indicated in the table.

4.2.1 Light curves and fitting

In figure 9 we show the light curve data points normalized to the reference model for the different energy ranges alongside the inputted temporal decay, with the light curve having been extracted from the simulated detection flux points. The parameters of Mrk 421, energy ranges and parameters of the observation are the ones given in section 3.3. The gap in observations seen in the figure corresponds to day time, and for the higher energy bins, the data points that notably differ from the inputted time decay indicate the upper limits (cases where the source could not be detected).

Additionally, to the expected detection flux points, not the light curve, we have performed a fitting to regain the original introduced spectrum. The obtained parameters for each simulation are shown as a result in the github code, and are not provided here. The $-\log(\mathcal{L})$ for each fitting are the results which are used, for each set, in figure 10 in the next section. As commented, the results at every gammapy simulation vary slightly because of the random seed it is initialized with. Nonetheless, the variations are negligible when comparing the differences amongst different layouts.

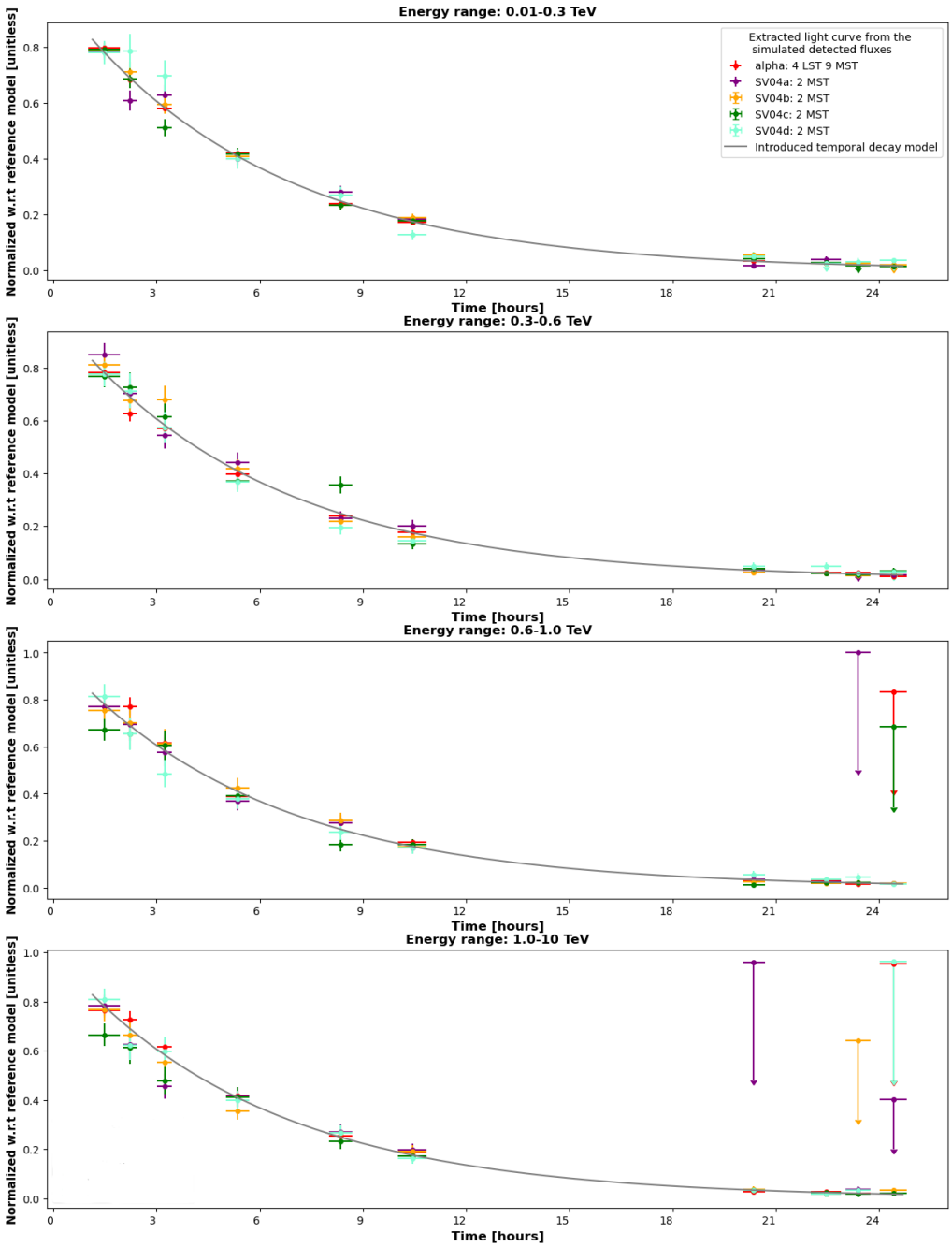

Figure 9: Extracted light curves from the simulated detection fluxes of Mrk 421 with the parameters described in section 3.3. The values are given for the Alpha configuration and four different 2 MSTs monitoring layouts, with their values normalized to the reference model and the inputted time decay.

4.2.2 Overall complementary-monitoring trade-off analysis

In figure 10 we can see the final comparison for all monitoring-complementary array pairs detailed in table 3. In the figure we can clearly see the expected trade-off between monitoring and complementary array performance, as if we gain performance in one sub-array, we loss performance in the other. The monitoring-complementary array pair that is marked as a good trade-off candidate corresponds to the monitoring array of SV05b in [7] notation. It has been highlighted as we do not observe a drop in the PPUT value (complementary array performance) when comparing it with those using only 2 MSTs for monitoring (blue dots), and it already provides an increase in monitoring array performance when comparing it to the 2 MSTs-monitoring layouts. Additionally, it obtains similar monitoring layout performances when comparing it to the others that also use 3 MSTs for monitoring.

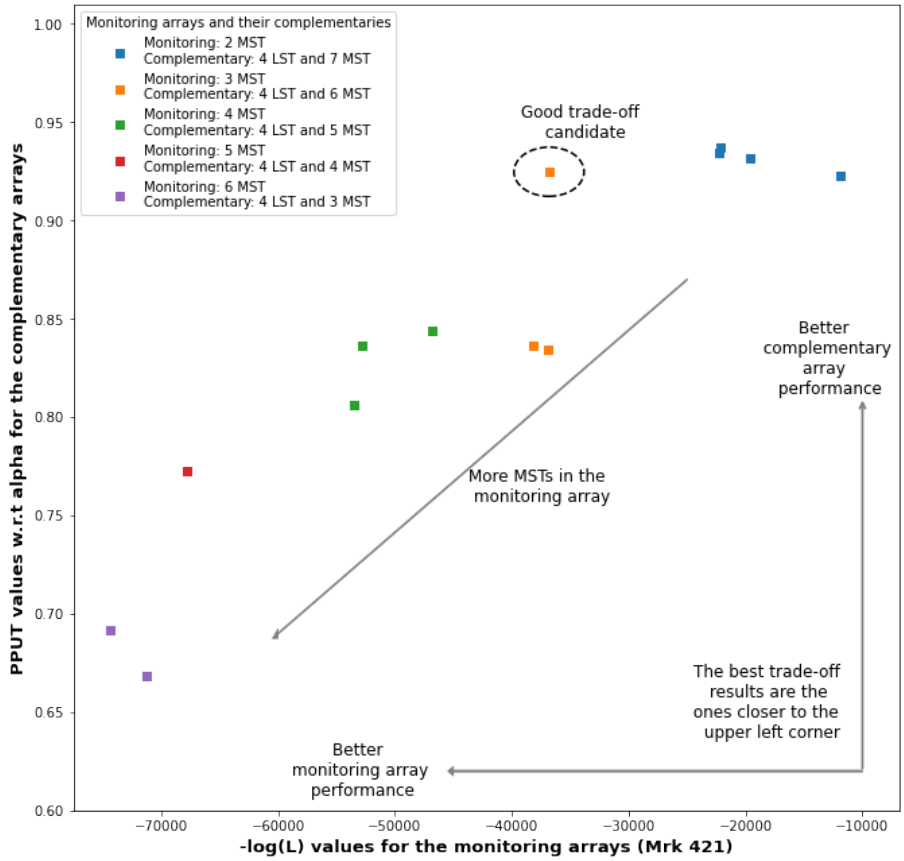

Figure 10: Trade-off between high monitoring array performance (x-axis, better performance to the left, smaller -log($\mathcal{L}$)) and small loss of complementary array performance (y-axis, better performance to the top, high PPUT values). We show the results for all tried monitoring-complementary array pairs (detailed in table 3), showcasing in the same colors the monitoring arrays that have the same number of MSTs.

5 Conclusions

The first goal addressed by this project was to provide a pipeline to perform a science verification study for the different construction phases in the CTAO northern hemisphere site. After devising the code, we have tested its working comparing different sub-arrays, checking that it gave sensible performance estimates and comparisons. Nonetheless, the northern CTAO site has an established small number of telescopes set to be built, and the construction set-up has many restrictions due to environmental constraints. For this reason, conducting a detailed analysis for this site will not provide a meaningful scientific impact, as it is unlikely we will be able to alter the already defined order of construction. Hence, it would be useful to apply the devised pipeline to the southern hemisphere site, where we might have more influence in the order of construction. To do so, the corresponding Monte Carlo simulations should be run, to then extract the IRFs and sensitivities from them and be able to compare performances.

The second goal of this project was to devise a pipeline to establish which monitoring layout will present the highest performance to monitor a certain variable source flare, while also seeking to limit the loss of performance for the complementary array left to perform regular observations. We have shown the results for a Mrk 421 long flare, and established a preferred candidate taking into account the required criteria. This procedure can now be applied to establish which monitoring layout will be most useful to study a certain variable source, as the results cannot be considered for general cases, given that they will depend on the variable source and flare characteristics we are aiming to detect. On this matter, here we have presented the results for a strong AGN with a long decay flare. Now, with the code published on the github link (Summer Project), we can also study, for instance, what would the results be if we aimed to observe a faint source with a short decay.

Acknowledgements

I would like to thank the organising team of the DESY Summer School for making this project possible, especially to Dr. Gernot Maier and Sarah Seibt.

I would also like to show my deep gratitude to Dr. Victor Barbosa, Dr. Orel Gueta and Dr. Gernot Maier, who have kindly guided and supervised this work, providing counsel and corrections through out all its stages.

Finally, I would like to express my appreciation to all the other summer interns.

References

[1] J. Myers. "Fermi Gamma-ray Space Telescope." (2023), [Online]. Available: https://fermi.gsfc.nasa.gov.

[2] "HAWC: the High-Altitude Water Cherenkov Observatory." (2023), [Online]. Available: https://www.hawc-observatory.org.

[3] "H.E.S.S. - the high energy stereoscopic system." (), [Online]. Available: https://www.mpi-hd.mpg.de/HESS/pages/about/.

[4] "The MAGIC telescopes." (2023), [Online]. Available: http://magic.mppmu.mpg.de.

[5] CTAO. "Cherenkov telescopes array." (2016), [Online]. Available: https://www.cta-observatory.org.

[6] H. Prokoph, "Investigations on gamma-hadron separation for imaging Cherenkov telescopes exploiting the time development of particle cascades," *Diploma Thesis Master's Degree Lepizig University*, 2009.

[7] G. Maier. "North-layouts-sv." (2023), [Online]. Available: https://gitlab.desy.de/cta/layouts/-/blob/main/North-Layouts/North-Layouts-SV.md.

[8] C. Nigro, "Evolution of data formats in very-high-energy gamma-ray astronomy," *Universe*, vol. 7, no. 10, p. 374, DOI: https://doi.org/10.3390/universe7100374.

[9] K. Bernlöhr, "Simulation of imaging atmospheric cherenkov telescopes with CORSIKA and sim telarray," *Astroparticle Physics*, vol. 30, no. 3, pp. 149–158, 2008. DOI: https://doi.org/10.1016/j.astropartphys.2008.07.009.

[10] K. Bernlöhr, *CTAO Simulation Telescope Models for CORSIKA and sim_telarray - prod5*, version 1.0.0, Zenodo, Feb. 2022. DOI: 10.5281/zenodo.6218687. [Online]. Available: https://doi.org/10.5281/zenodo.6218687.

[11] M. Linhoff, "Python open-source package *pyirf*," 2023. DOI: https://doi.org/10.5281/zenodo.8277216.

[12] *Cherenkov Telescope Array Observatory and Cherenkov Telescope Array Consortium. CTAO Instrument Response Functions - prod5 version v0.1*, version v0.1, Zenodo, Sep. 2021. DOI: 10.5281/zenodo.5499840. [Online]. Available: https://doi.org/10.5281/zenodo.5499840.

[13] P. Cumani, "Baseline telescope layouts of the cherenkov telescope array," *Proceedings of the 35th International Cosmic Ray Conference (ICRC 2017)*, 2017. DOI: https://doi.org/10.48550/arXiv.1709.00206.

[14] C. Deil, "Gammapy - a prototype for the CTA science tools," 2017. DOI: https://doi.org/10.48550/arXiv.1709.01751.

[15] C. Nigro, "Towards open and reproducible multi-instrument analysis in gamma-ray astronomy," *A & A*, vol. 625, A10, 2019. DOI: https://doi.org/10.1051/0004-6361/201834938.

[16] S. Wakely, "Tevcat: An online catalog for very high energy gamma-ray astronomy," *Proceedings of the 30th International Cosmic Ray Conference*, vol. 3, pp. 1341–1344, 2008. [Online]. Available: https://articles.adsabs.harvard.edu/pdf/2008ICRC...30c1341W.

[17] "Gammapy documentation: Fitting." (2023), [Online]. Available: https://docs.gammapy.org/dev/tutorials/api/fitting.html.